Research Article | Vol. 17, No. 5 / 1 May 2026 / Biomedical Optics Express 2467
Biomedical Optics EXPRESS

Five-modal multiphoton microscopy enabled by a tunable dual-wavelength fiber laser

LIHAO ZHANG,[1,2,†] RUNZHI CHEN,[3,4,†] XINYI WANG,[5] QI SUN,[5] PING XUE,[4,7] GANG JING,[6,8] AND GUOQING CHANG[1,2,9]

[1]*Beijing National Laboratory for Condensed Matter Physics, Institute of Physics, Chinese Academy of Sciences, Beijing 100190, China*
[2]*University of Chinese Academy of Sciences, Beijing 100049, China*
[3]*Innovation Center for Laser Medical Instruments, Shenzhen Tsinghua University Research Institute, Shenzhen 518057, China*
[4]*Department of Physics, Tsinghua University, Beijing 100084, China*
[5]*Department of Cell Biology, School of Basic Medical Sciences, Peking University Stem Cell Research Center, Peking University Health Science Center, Peking University, Beijing 100191, China*
[6]*Shenzhen Key Laboratory of Opto-Mechatronics, Shenzhen Tsinghua University Research Institute, Shenzhen 518057, China*
[7]*xuep@tsinghua.edu.cn*
[8]*jingg@tsinghua-sz.org*
[9]*guoqing.chang@iphy.ac.cn*
[†]These authors contributed equally.

Abstract: Coherent anti-Stokes Raman scattering (CARS) microscopy provides chemically specific, label-free contrast that complements the structural and functional information offered by multiphoton microscopy (MPM). However, the widespread adoption of multimodal CARS systems has been hindered by the complexity and limited tunability of conventional solid-state laser sources. We demonstrate a tunable dual-wavelength laser source based on self-phase-modulation enabled spectral selection (SESS), delivering pump pulses tunable from 775 nm to 950 nm together with synchronized Stokes pulses at 1.035 µm. The source operates at a repetition rate of 37 MHz with pulse energies exceeding 2 nJ and enables continuous Raman shift coverage from 800 cm^{-1} to 3500 cm^{-1}. By integrating this CARS excitation source with multiphoton excitation channels, we demonstrate a five-modal MPM platform; that is, CARS, two-photon excited fluorescence (2PEF), three-photon excited fluorescence (3PEF), second-harmonic generation (SHG), and third-harmonic generation (THG). Multimodal imaging of mouse brain slices demonstrates chemically selective visualization of lipids and unsaturated fatty acids, together with complementary structural and metabolic contrasts.

1. Introduction

Multiphoton microscopy (MPM) imaging has become a key tool in biomedical research due to its capability of non-invasive acquisition of structural and functional information without labeling [1]. Utilizing the nonlinear interaction between ultrashort laser pulses and biological samples, MPM imaging enables various label-free nonlinear imaging processes, including two-photon excited fluorescence (2PEF), three-photon excited fluorescence (3PEF) [2,3], second-harmonic generation (SHG), and third-harmonic generation (THG) [4–9]. These modalities provide rich contrast for observing tissue morphology, cellular metabolic activity, and specific microstructures (*e.g.*, collagen fibers, cell interfaces). However, these modalities typically lack the inherent ability for chemically specific imaging, *i.e.*, the capability to directly identify specific chemical components based on the molecular vibrational "fingerprint." In this context, coherent anti-Stokes Raman scattering (CARS) microscopy—another MPM imaging modality—emerged as a powerful solution for label-free chemical imaging [10,11]. CARS generates a frequency-upconverted

#588809 https://doi.org/10.1364/BOE.588809
Journal © 2026 Received 2 Jan 2026; revised 19 Feb 2026; accepted 31 Mar 2026; published 16 Apr 2026

Biomedical Optics EXPRESS

signal whose intensity is significantly higher than spontaneous Raman scattering, making it easier to detect with conventional detectors, thus laying a solid foundation for high-speed chemical imaging. By detecting the unique vibrational spectra of molecules, CARS enables in-situ identification and direct imaging of specific chemical components (*e.g.*, lipids, proteins) in biological tissues [12–16], thereby serving as a powerful complement to the aforementioned structural MPM modalities. However, integrating high-performance CARS technology with other nonlinear modalities on a compact platform has been challenging primarily due to limitations in the driving laser source. The driving source must provide dual-wavelength ultrashort pulses that are precisely synchronized. The source should have a high repetition-rate (typically >30 MHz) to ensure fast image acquisition. For targeted imaging of different chemical bonds, the source must possess broad and flexible wavelength tuning capability to cover key molecular vibrational spectral regions (typically referring to the Raman shift range of 800–3500 cm^{-1}). To balance high spectral resolution with substantial signal strength, the pulse duration is typically optimized to the picosecond range, aiming to suppress the non-resonant background while achieving efficient nonlinear excitation [17].

Most CARS driving sources are derived from solid-state lasers (*e.g.*, Ti:Sapphire lasers). However, these systems are typically bulky, expensive, sensitive to environmental vibrations and temperature fluctuations, and have relatively poor stability. These drawbacks greatly hinder the promotion and application of CARS imaging in clinical environments. In contrast, ultrafast fiber lasers provide an ideal platform for moving CARS imaging from the laboratory to the clinical setting due to their inherent advantages of excellent environmental stability, superior beam quality, compactness, and ease of maintenance. Depending on the dopant of the gain fiber, ultrafast fiber lasers usually work at three wavelength ranges; that is, ultrafast Yb-fiber lasers at ~1.03 µm, ultrafast Er-fiber lasers at ~1.55 µm, and ultrafast Tm-fiber or Ho-fiber lasers at ~2.0 µm. However, their gain bandwidth usually limits the intrinsic spectral coverage to <50 nm.

Dual-wavelength excitation for CARS therefore requires integrating fiber lasers with nonlinear wavelength-conversion schemes. Three representative routes have been explored: fiber-based optical parametric oscillators (OPO) [18–24], supercontinuum generation (SCG) [25–28], and dual-wavelength fiber oscillators/amplifiers.

In 2020, Brinkmann et al. demonstrated a portable all-fiber dual-wavelength picosecond source with wide tunability based on a fiber OPO [29], enabling rapid all-electronic tuning over >2700 cm^{-1} with high output power. However, the long photonic-crystal fiber can introduce elevated intensity noise and may require additional suppression (e.g., auto-balanced detection) for optimal sensitivity [30]. Moreover, the picosecond pulse duration, while beneficial for spectral resolution, is less compatible with femtosecond-driven modalities (SHG, THG, 2PEF), which can complicate tightly synchronized multimodal integration.

Another approach relies on fiber nonlinearities to generate SCG that covers the required wavelengths. In 2018, Shen *et al.* reported the generation of a picosecond SCG extending beyond 1600 nm in large-mode-area photonic crystal fibers for CARS, achieving microjoule-level pulse energy and Watt-level average power [31]. However, this improvement of pulse energy came at the cost of a lower repetition rate at 1 MHz, which significantly limits the imaging speed. Furthermore, SCG originates from complicated nonlinear interaction between the input pulse and the host fiber material, and it is difficult (if not possible) to tailor a SCG spectrum such that most energy concentrates at the wavelength desired by CARS imaging.

The third approach is to construct a dual-wavelength fiber laser system that consists of fiber amplifiers working at different wavelengths to boost pulse energy [32–35]. This architecture offers inherent temporal synchronization and potentially lower intensity noise. For example, Freudiger *et al.* utilized an Er-doped oscillator to provide seed pulses at 1.55 µm. One portion was spectrally broadened in a highly nonlinear fiber and the spectral component at 1.03 µm was selected to be amplified in a Yb-doped fiber, which served as the Stokes pulse. The other

Biomedical Optics EXPRESS

portion was amplified in an Er-doped fiber and then frequency-doubled in a periodically poled lithium niobate (PPLN) crystal to generate the ~0.79-μm pump pulse [32]. Although this system demonstrated excellent stability and low noise, the wavelength tuning range was primarily confined to the high-wavenumber region (2800-3100 cm^{-1}), limiting its application in broader chemical imaging encompassing the fingerprint region. To expand the wavelength coverage, fiber-optic nonlinear wavelength conversion has to be implemented in at least one branch of the two-wavelength fiber laser system.

In 2019, Zach *et al.* reported a dual-wavelength (1.03 μm/1.55 μm) fiber laser, and the 1.55-μm pulse was amplified in a 15-meter-long Er-doped fiber with very large mode-area; soliton self-frequency shift (SSFS) in the fiber produced ultrashort pulses with the center wavelength tunable from 1.62 μm to 1.99 μm [34]. These redshift pulses were subsequently frequency-doubled using a PPLN crystal to obtain the pump pulses tunable from 810 nm to 990 nm. This system integrated the dual-wavelength laser with nonlinear wavelength conversion, which significantly extended the wavelength tuning range. However, the SSFS in the long fiber converted relative intensity noise into large relative timing jitter between the pump pulse and the Stokes pulse, which in turn degraded the imaging quality. In 2020, Cao et al. followed the aforementioned method to obtain a dual-wavelength (1.06 μm/1.55 μm) system and then utilized the 1.55-μm pulse combined with SCG to produce an excitation bandwidth exceeding 4000 cm^{-1}, fully covering the vibrational spectrum from the fingerprint region to the high-wavenumber region. Its all-polarization-maintaining fiber structure endowed the system with high environmental stability, However, the laser system employed SCG to provide such a broad bandwidth and inherently suffered from low spectral power density and high intensity noise, which may constrain the achievable signal-to-noise ratio in practical imaging [35].

Among fiber-optic methods to produce wavelength tunable pulses, self-phase-modulation (SPM) enabled spectral selection (SESS) is of particular interest. The essence of SESS is to ensure that SPM dominates the spectral broadening such that the broadened spectrum consists of well-isolated spectral lobes; filtering the leftmost/rightmost spectral lobes generates wavelength tunable femtosecond pulses [36]. SESS exhibits excellent energy scalability; using large-mode-area fiber with short length generated SESS pulses with up to 100-nJ energy [37]. SESS relies on short fiber with minimal dispersion, and the generated pulses acquire a relative timing jitter that has been experimentally shown to be at least an order of magnitude lower than that of SSFS under comparable conditions [38]. In this paper, we incorporate SESS into the 1.55-μm branch of a home-built dual-wavelength (1.03 μm/1.55 μm) fiber laser, which generates ultrashort pulses tunable from 1.55 μm to 1.95 μm. After frequency doubling in a BBO crystal, the resulting pulses serve as the pump tunable in the wavelength range of 775–950 nm; together with the Stokes pulses offered by the 1.03-μm branch, this laser source allows CARS imaging with a wavenumber difference covering 800–3500 cm^{-1}. We also combine CARS with SHG, THG, 2PEF, and 3PEF, and demonstrate a biomedical MPM system with five imaging modalities.

To facilitate a quantitative comparison among multiphoton microscopes incorporating coherent Raman scattering imaging modality, Table 1 summarizes key performance parameters (e.g., Raman tuning range, repetition rate, pulse duration, and output power) of representative reported systems.

Although five-modal multiphoton imaging has been demonstrated previously [39], such implementations typically rely on supercontinuum generation and free-space pulse shaping. In contrast, the present work achieves five-modal integration using a compact dual-wavelength fiber architecture with inherent synchronization.

Biomedical Optics EXPRESS

Table 1. Quantitative comparison of representative multimodal multiphoton microscopes that consists of coherent Raman scattering imaging modality

	Modalities	Wavelength (nm)	Rep. rate (MHz)	Power (mW)	Design emphasis
This work	SHG/THG/2PEF/3PEF/CARS	Pump:775-950 Stokes: 1030 MPM: 1100	37	80	Multimodal integration, Broad Raman coverage, Fiber-centric architecture
[30]	SRS	Pump: 946-775 Stokes: 1053-1027	40.5	46	All-fiber, Limited modality diversity
[31]	CARS	Pump: 1064 Stokes: 1100-1600	1	9	SC-based, Low repetition rate
[32]	SRS	Pump: 790 Stokes: 1015-1045	59	1700	Dual-wavelength amplification, Narrow Raman coverage
[34]	SHG/THG/2PEF/CARS	Pump: 810-1000 Stokes: 1620-1990	80	45	Dual-wavelength amplification, All-fiber SSFS,
[39]	SHG/THG/2PEF/3PEF/CARS	SCG: 780-1300	80	32	SCG followed by pulse shaping, Free-space bulk system

2. CARS imaging setup

Figure 1 shows a schematic of the CARS imaging setup, which comprises a laser source derived from a dual-wavelength fiber laser and a scanning microscope.

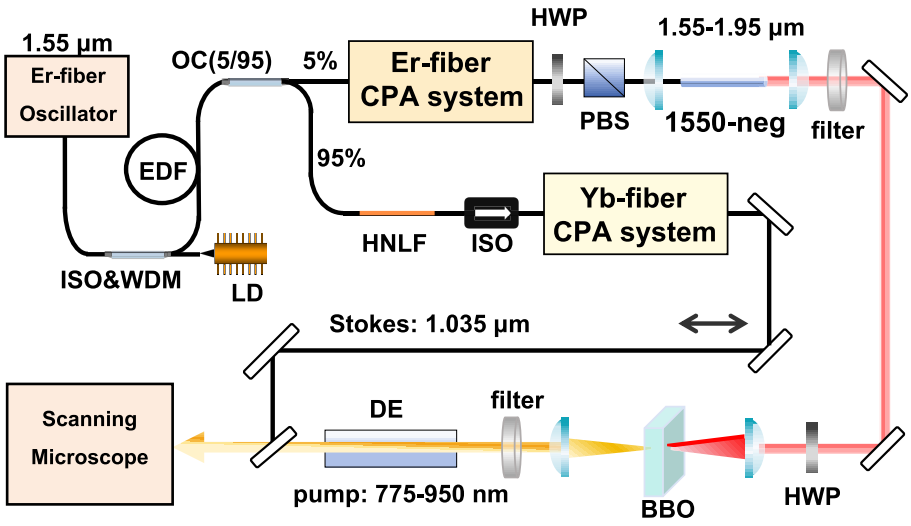

Fig. 1. Schematic of the tunable dual-wavelength light source driving CARS. ISO: isolator, WDM: wavelength division multiplexer, LD: laser diode, EDF: erbium-doped fiber, OC: output coupler, HNLF: highly nonlinear fiber, DE: dispersion element, HWP: half-wave plate, PBS: polarizing beam splitter, BBO: BaB_2O_4 crystal, and DM: dichroic mirror.

The CARS laser source uses a saturable absorber mode-locked Er-fiber oscillator as the seed source, which delivers 1.55-μm pulses at a repetition rate of 37 MHz with 1.3-mW average power. The seed pulses are then amplified in the polarization-maintaining (PM) Er-fiber (Er80-4/125-HD-PM, nLIGHT) in a nonlinear manner such that the optical spectrum is substantially broadened mainly by SPM. A 10-cm single-mode PM fiber (PM1550-XP, Nufern) is then used

Biomedical Optics EXPRESS

to de-chirp the amplified pulses to 33 fs in duration with an average power of 76 mW. The de-chirped pulses are separated into two branches after passing through a 5/95 output coupler, and 95% of them are coupled into a highly nonlinear fiber (HNLF) to derive the Stokes pulse for CARS imaging. Significant nonlinear effects in the HNLF broadens the pulse spectrum and the short-wavelength side reaches 1.0 µm [blue solid curve in Fig. 2(a)]. We then use a fiber-pigtailed isolator as a low-pass optical filter to select the leftmost spectral lobe shown as the red dashed curve in Fig. 2(a). The filtered spectrum is then fed into a Yb-fiber Chirped Pulse Amplification (CPA) system that is composed of a fiber stretcher, cascaded fiber amplifiers, and a grating-pair compressor. We use 40-m single-mode PM fiber (PM980C-HP, Nufern) serving as the stretcher that provides a total dispersion of 1.92 ps/nm. The stretched pulses are then amplified to 6.3 W in average power by a single-mode Yb-fiber (Yb401, CorActive) amplifier cascaded by a large-mode-area Yb-fiber (LMA-YDF-30/250-HI-8, Nufern) amplifier. The blue curve in Fig. 2(b) plots the spectrum of the amplified pulses with the center wavelength at 1.035 µm. The amplified pulses are then compressed by a pair of diffraction gratings (1000 lines/mm); the compressed pulses have an average power of 5 W. We use an intensity autocorrelator to measure the compressed pulse duration. As the measured autocorrelation trace [Inset of Fig. 2(b)] shows, the pulse duration (full width at half maximum, FWHM) is estimated to be 175 fs with an assumption of a hyperbolic secant profile.

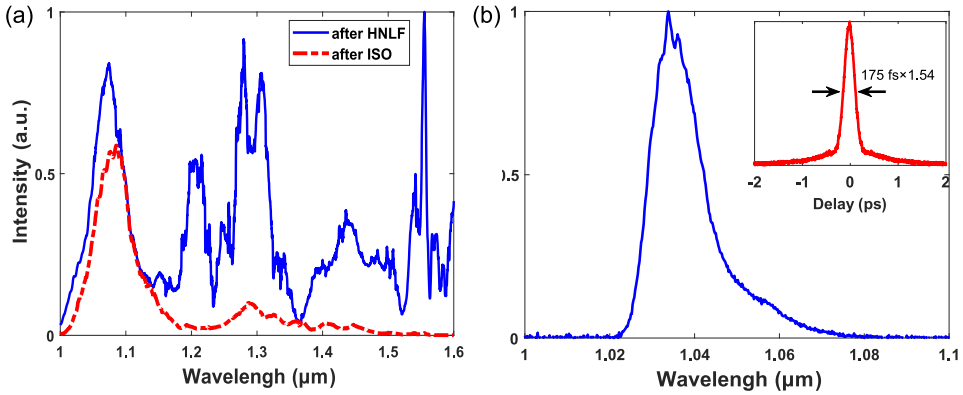

Fig. 2. (a) Broadened spectrum after HNLF (blue solid curve) and filtered spectrum after ISO (red dashed curve). (b) spectrum at the output of Yb-fiber CPA system. Inset: measured autocorrelation trace of the compressed pulses.

To obtain pump pulses for CARS imaging, 1.55-µm pulses at the 5% port of the output coupler is seeded into a Er-fiber CPA system also consisting of a fiber stretcher, cascaded Er-fiber amplifiers, and a grating-pair compressor. The fiber stretcher is implemented using 15-m dispersion-compensation fiber (DM1012-A, YOFC) in a double-pass configuration and provides a total dispersion of 4.2 ps/nm. After two stages of pre-amplification based on single-mode Er-fibers (Er80-4/125-HD-PM and Er80-8/125-PM, nLIGHT), the pulses are further amplified in an Yb/Er co-doped large-mode-area fiber (PLMA-EYDF-25P/300-XPH-11FA, Nufern) to an average power of 6.5 W. As the blue curve in Fig. 3 shows, the spectrum of the amplified pulses centers at 1.55 µm. A pair of diffraction gratings (996 lines/mm) are used to compress the amplified pulses and the compressed pulses have an average power of 5.2 W. The measured autocorrelation trace (red curve in the inset of Fig. 3) shows that the compressed pulse duration (FWHM) is about 270 fs assuming a hyperbolic secant profile.

The compressed 1.55-µm pulses are coupled into a 9.6-cm fiber with a mode-field diameter of 4 µm (1550-neg, YOFC) for SESS. A half-wave plate (HWP) and a polarizing beam splitter (PBS) are used to adjust the pulse energy coupled into the fiber. The fiber has a low dispersion of

Biomedical Optics EXPRESS

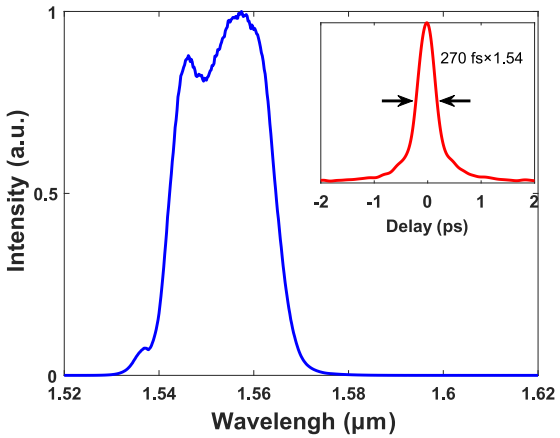

Fig. 3. spectrum at the output of Er-fiber CPA system. Inset: measured autocorrelation trace of the compressed pulses.

−1 ps/nm/km at 1.55 μm such that SPM dominates the spectral broadening and the broadened spectrum comprises separated spectral lobes [40]. As we increase the coupled pulse energy into the fiber, the rightmost spectral lobe continuously shifts from 1.6 μm to 1.95 μm. We use a suitable bandpass filter to select these spectral lobes with a 50-nm wavelength step and plot them in Fig. 4. These spectra give rise to wavelength-tunable pulses with the average power varying between 394 mW and 680 mW (corresponding to a pulse energy variation of 11-18 nJ).

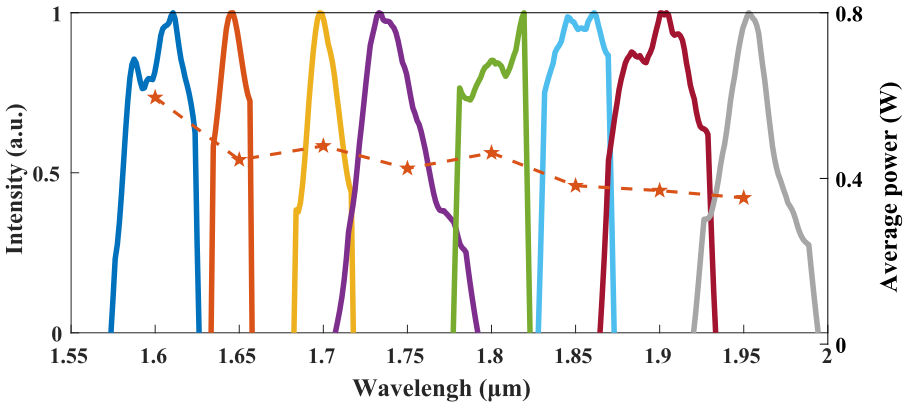

Fig. 4. Representative spectra by filtering the rightmost spectral lobe of the broadened spectrum in the nonlinear fiber (1550-neg), and their average power.

After collimation by an aspheric lens, the SESS pulses are focused into a 2-mm-thick BBO crystal (Type II phase matching) for frequency doubling to produce the CARS pump pulses. Figure 5 presents five typical spectra of the pump pulses with the center wavelength set at 775 nm, 788 nm, 800 nm, 880 nm, and 937 nm to target distinct molecular vibrations. When combined with the fixed Stokes pulse at 1.035 μm, the pump pulses at these five wavelengths allow probing the Raman shifts of 3250 cm^{-1} (O–H stretching of water), 3015 cm^{-1} (=C–H stretching of unsaturated fatty acids), 2840 cm^{-1} (–C–H stretching of lipids), 1700cm^{-1} (amide I band of proteins), and 1001 cm^{-1} (O-P-O stretching of DNA). In other words, our laser source enables selective CARS imaging targeting characteristic vibrational modes of key cellular constituents, including water, lipids (with specific access to unsaturated fatty acids), proteins, and nucleic acids.

Biomedical Optics EXPRESS

The average power of pump pulses ranges between 80 mW and 160 mW, and the corresponding pulse energy exceeds 2 nJ, which meets the pulse energy and repetition-rate requirements for efficient CARS microscopy and falls within the commonly adopted tens-of-MHz regime for MPM. The reported power values reflect the output capability of the excitation source rather than mandatory operating conditions; in practical imaging, the delivered power at the sample can be readily attenuated according to experimental requirements. The long-term power stability was evaluated at the output port before entering the scanning microscope under typical laboratory conditions. Continuous monitoring over a 4-hour period showed a power fluctuation within ~3%, confirming the stability of the excitation source for extended imaging experiments. To use the spectral focusing technique to increase spectral resolution during the imaging [16, 41,42], both the pump and Stokes pulses are temporally stretched to ~3 ps using a grating-pair-based dispersion compensation setup. After passing through an adjustable optical delay line, the Stokes pulses are combined with the pump pulses at a dichroic mirror and the combined pulses are directed into a scanning microscope.

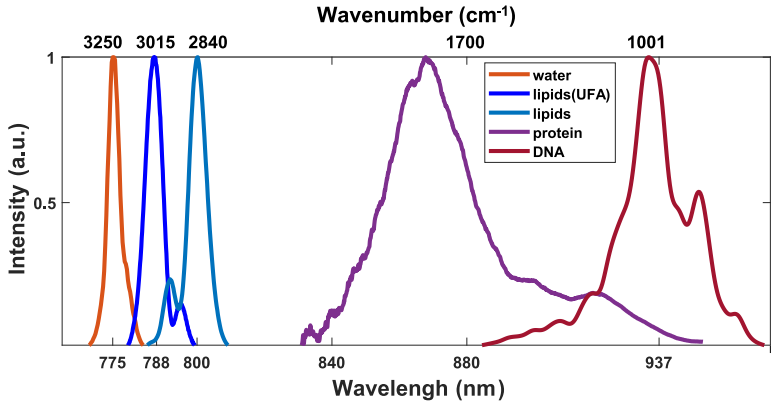

Fig. 5. Five typical spectra centered at 775 nm, 788 nm, 800 nm, 880 nm, and 937 nm to target distinct molecular vibrations corresponding to Raman shifts of 3250 cm^{-1} (O–H stretching of water), 3015 cm^{-1} (=C–H stretching of unsaturated fatty acids), 2840 cm^{-1} (–C–H stretching of lipids), 1700 cm^{-1} (amide I band of proteins), and 1001 cm^{-1} (O-P-O stretching of DNA).

The scanning microscope (MPM-2PKIT, Thorlabs) comprises a scanning unit, a relay lens module, an imaging objective, and a collection module. The combined pump-Stokes beam from the CARS laser source is initially deflected by a resonant scanner (LSKGR08, Thorlabs) operating at a fixed frequency of 8 kHz. It is subsequently expanded by a factor of four using a scan lens (SL50-2P2, Thorlabs) and a tube lens (TL200-2P2, Thorlabs), and then directed toward the imaging objective. A high-numerical-aperture (NA = 1.05) water-immersion objective (XLPLN25XWMP2, Olympus) is employed to focus the pump and Stokes pulses onto the biological sample and to collect the generated CARS signal in the epi-direction. The collected signal passes through a bandpass filter and is detected by a photomultiplier tube (PMT2100, Thorlabs). The system utilizes interchangeable filter modules and each module contains a dichroic mirror and bandpass filters, which allows configuration for specific spectral ranges of interest based on the sample. To minimize noise from ambient light given the high sensitivity of the photomultiplier tube, we operate the microscope in a darkened environment. With image resolution maintained, the system supports video-rate imaging at up to 30 frames per second for a 512×512-pixel format. In the present configuration, the measured imaging speed exceeds 30 frames per second, which was further verified via external video recording. The maximum

Biomedical Optics EXPRESS

optical scan angle of the resonant mirror is limited to ±5°, corresponding to a maximum field of view of $800 \times 800\ \mu m^2$.

3. CARS imaging verification based on polystyrene microspheres

Before imaging complex biological samples, we first quantitatively evaluate the spatial resolution of the constructed CARS microscope using standard polystyrene microspheres. A solution of polystyrene microspheres with a diameter of approximately 500 nm is diluted 1:100, dropped onto a glass slide, and allowed to air dry naturally. The microspheres accumulate at the edge of the droplet forming a ring-shaped enriched area. These microspheres have a significant Raman characteristic peak near 3045 cm^{-1} [43]. Therefore, we precisely tune the pump wavelength to 787 nm, making the pump-Stokes wavenumber difference resonant with this characteristic peak.

Figure 6(a) shows the CARS image of the aggregated distribution of polystyrene microspheres in a 30 μm × 30 μm field of view. The image shows uniform signals and high contrast, indicating good excitation efficiency. The region of interest marked by the white square in the figure is magnified and shown in Fig. 6(b). We extract the signal intensity distribution along the transverse diameter of a microsphere [black curve in Fig. 6(c)], and the FWHM is estimated as ~0.8 μm via Gaussian fitting [blue curve in Fig. 6(c)], which is consistent with cellular-level coherent Raman imaging reported in representative fiber-based and conventional platforms. This result confirms that our dual-wavelength laser source possesses excellent spatial mode quality and precise spatiotemporal synchronization such that the CARS microscope can achieve high-resolution, label-free imaging.

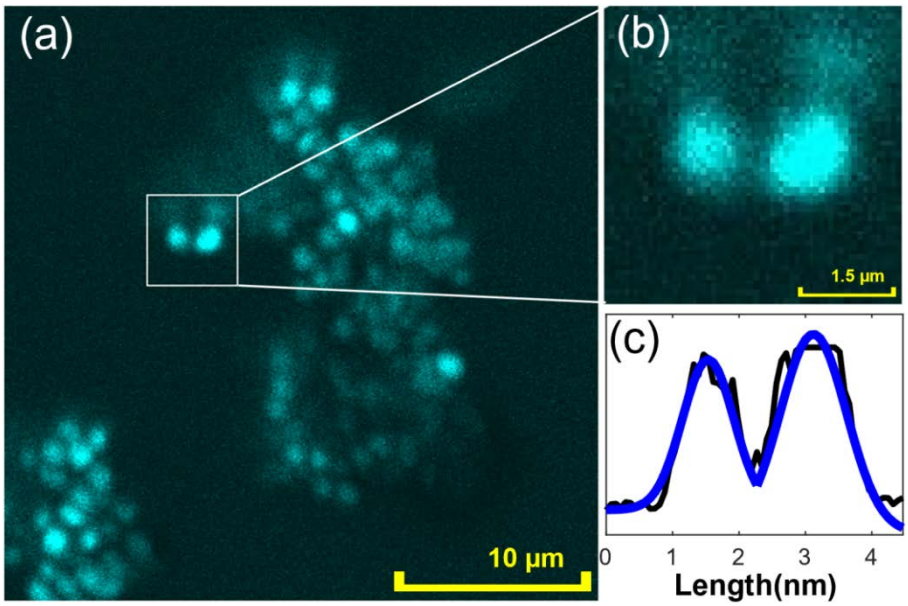

Fig. 6. (a) CARS image of 500-nm-diameter polystyrene microspheres at a wavenumber difference of 3045 cm^{-1}. (b) Magnified image of white square area in (a). (c) Signal intensity profile (black curve) along the transverse direction of the microsphere in (b) and Gaussian fit (blue curve).

4. Multimodal MPM imaging of mouse brain slices

We have previously developed a pre-chirp and gain-managed Yb-fiber laser to achieve simultaneous label-free autofluorescence-multiharmonic microscopy, integrating four nonlinear modalities:

Biomedical Optics EXPRESS

2PEF, 3PEF, SHG, and THG. This system has enabled label-free imaging of cellular and extracellular structures in human tissues such as intestinal and lung adenocarcinomas [44]. To add chemical specificity, we now combine above developed dual-wavelength CARS source with the pre-chirp and gain-managed Yb-fiber laser via a dichroic mirror. The scanning microscope driven by this combined source allows MPM imaging with five modalities, *i.e.*, CARS, 2PEF, 3PEF, SHG, and THG. We prepare 5-µm-thick paraffin-embedded coronal sections of mouse brain to demonstrate this multimodal imaging capabilities by imaging mouse brain sections in the third ventricle (D3 V) and arcuate hypothalamic nucleus (ARC) regions in order to visualize lipid distribution, trace metabolic activity, and identify collagen structures and cellular interfaces in a multiscale, label-free manner.

4.1. Imaging of –C–H stretching (2840 cm^{-1}) in the D3V

As a core periventricular organ within the hypothalamus, the D3 V functions as a critical hub for the brain to sense systemic circulatory status and coordinate systemic metabolic and endocrine responses. Its physiological roles encompass energy balance, thermoregulation, and neuroendocrine integration. To elucidate the mechanisms underlying these precise regulatory functions, it is essential to investigate both the D3 V cytoarchitecture as well as its chemical composition at the molecular level with a specific focus on lipid distribution and status. Lipids constitute the fundamental structural framework of cell membranes, serve as the primary form of energy storage, and act as precursors for numerous signaling molecules; consequently, their metabolism and dynamics directly influence neuronal excitability, synaptic plasticity, and global energy homeostasis. Accordingly, we employ the chemical specificity of CARS microscopy to perform targeted imaging of the spatial distribution of lipids within the D3 V region. The symmetric stretching vibration of saturated –C–H bonds in lipid molecules exhibits a strong characteristic Raman signal at 2840 cm^{-1}, providing a unique "fingerprint" window for the label-free, in situ visualization of lipids within complex biological tissues. Specific imaging of lipid distribution in the D3 V is achieved by precisely tuning the pump wavelength to 800 nm (with 80-mW average power), thereby matching the wavenumber difference of 2840 cm^{-1} relative to the 1.035-µm Stokes pulses (with 40-mW average power). The CARS signal is subsequently isolated from both the pump and Stokes pulses using a bandpass filter with a center wavelength of 650 nm (FF01-650/13-25, Semrock).

Figure 7 presents multimodal MPM images of the D3 V, where Figs. 7(a-d) display the results of CARS, 2PEF, SHG, and THG imaging. The CARS image [Fig. 7(a)] clearly delineates lipid-rich domains consistent with structures such as myelin and synaptic vesicles, which supports studies of lipid metabolism and membrane dynamics. Simultaneously, the 2PEF signal captures endogenous fluorescence from NADH and FAD [Fig. 7(b)], where high signal density reflects active cellular metabolism consistent with the region's energy-demanding functions. The SHG channel shown in Fig. 7(c) displays a distinct pericellular collagen network likely corresponding to meningeal or vascular basement membranes that provide structural support. Figure 7(d) records the THG signal that originates from refractive-index interfaces (e.g., cell membranes and lipid droplets) and partially overlaps with CARS lipid maps yet lacking chemical specificity. The composite image in Fig. 7(e) that integrates CARS, 2PEF, SHG, and THG channels illustrates the multidimensional structural and chemical network within the D3 V. The imaging quality was further evaluated by deliberately detuning the temporal overlap between the pump and Stokes pulses to suppress the resonant contribution and estimate the noise floor; based on the signal and noise levels extracted from Fig. 7, the corresponding SNR was approximately 45 dB under typical imaging conditions. Together, these complementary modalities offer a label-free, multiscale view of the tissue while CARS image provides unique chemical specificity for in vivo studies of neurometabolic interactions.

Biomedical Optics EXPRESS

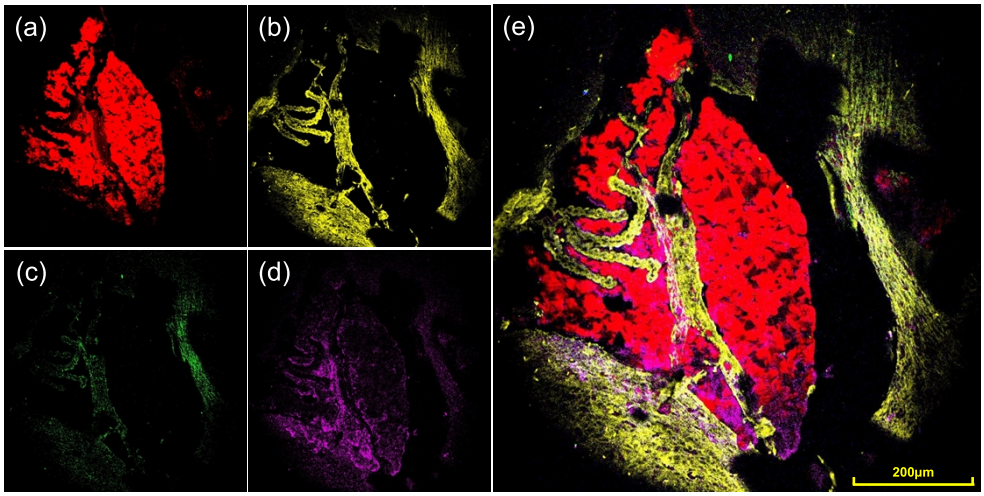

Fig. 7. Multimodal nonlinear imaging of D3 V region of mouse brain slice. (a) CARS: Specifically displays lipid distribution. (b) 2PEF: Originates from endogenous fluorophores (e.g., NADH/FAD). (c) SHG: Sensitive response to non-centrosymmetric structures, revealing the collagen fiber network in the tissue. (d) THG: Sensitive to refractive index interfaces, marking boundaries such as cell membranes and lipid droplets. (e) Fused image of the D3 V region, where different modalities in the same area complement each other.

4.2. Imaging of = C–H stretching (3015 cm^{-1}) in the ARC

Situated adjacent to the D3 V, the ARC represents another fundamental hub for metabolic control within the hypothalamus. It contains specialized neuronal populations that function as primary sensors for circulating metabolic signals, and play an indispensable role in the regulation of appetite, energy expenditure, and glucose homeostasis. Given its unique location and function, the ARC is highly sensitive to changes in the systemic metabolic state, making it a critical region for investigating the neural mechanisms of metabolic diseases. Within this neural microenvironment, unsaturated fatty acids (UFA) are of particular biological significance. Unlike saturated lipids that primarily serve as energy storage, UFA are essential components that determine the fluidity and permeability of neuronal cell membranes. Furthermore, they act as bioactive mediators in signaling pathways associated with neuroprotection, neuroinflammation, and oxidative stress. Therefore, the ability to selectively visualize UFA and distinguish their distribution from saturated lipids offers a key link in revealing how lipid composition affects brain structure and function, which is of potential relevance to studies of neurodegenerative diseases and metabolic disorders.

To achieve specific imaging of these molecules, we leverage the broad tunability of our SESS-enabled laser source to target the unique vibrational signature of UFA. The stretching vibration of the = C–H bond in unsaturated lipids exhibits a characteristic Raman peak at 3015 cm^{-1} [45]. To access this frequency, we precisely set the pump wavelength at 788 nm. When combined with the Stokes pulses centered at 1.035-μm, this configuration generates the required wavenumber difference of 3015 cm^{-1}. During the experiment, the excitation power is maintained at 90 mW for the pump pulses and 45 mW for the Stokes pulses. The resulting CARS signal is effectively isolated using a bandpass filter with a center wavelength of 637 nm.

Figure 8 presents multimodal imaging of the mouse brain ARC region with specific detection of unsaturated fatty acids (UFA). The CARS channel [Fig. 8(a)] specifically targets the = C–H bond vibration in UFA, accurately delineating their spatial distribution; contrasting this with saturated lipids provides critical evidence for assessing membrane fluidity and metabolic disorder-associated changes. The 2PEF and 3PEF signals [Figs. 8(b) and 8(d)] simultaneously capture endogenous

Biomedical Optics EXPRESS

fluorescence from metabolic cofactors such as NADH and FAD, and collectively map the cellular metabolic activity. The SHG image in Fig. 8(c) reveals a distinct pericellular collagen network that likely provides structural support, while the THG channel [Fig. 8(e)] offers structural contrast that partially overlaps with lipid-rich domains. The five-modal fused image in Fig. 8(f) integrates these complementary contrasts and illustrates the multidimensional architecture and chemistry within the ARC, which elucidates the complex "chemistry–structure–function" relationship in situ, with the CARS modality serving as a vital tool for decoding links between lipid metabolism and neural function.

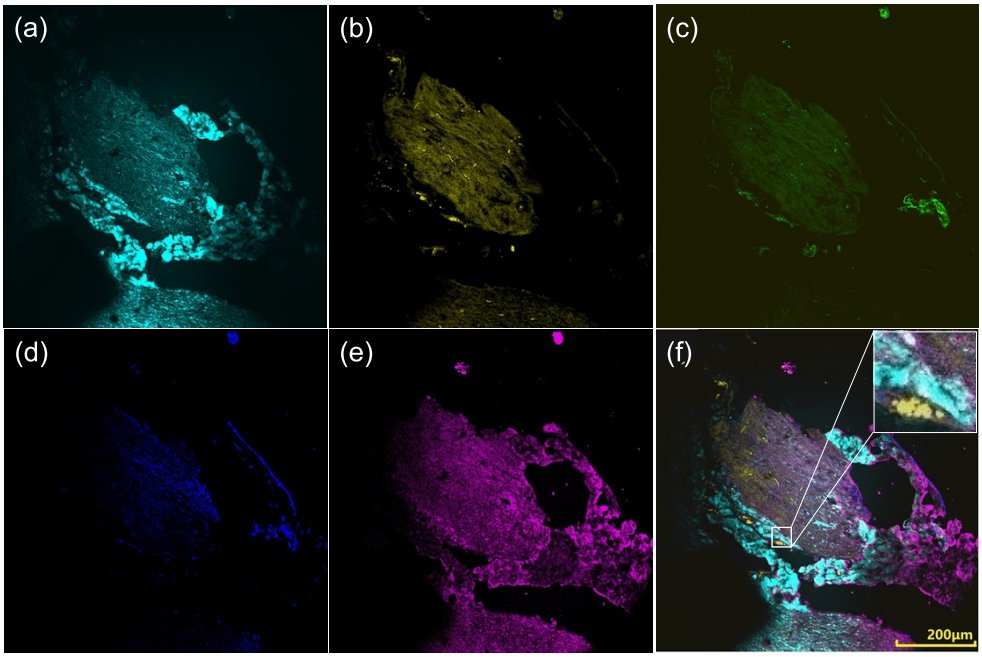

Fig. 8. Multimodal imaging of the mouse brain ARC region and specific detection of unsaturated fatty acids. (a) CARS: Specifically targets the = C–H bond vibration in UFA within lipid molecules, accurately revealing their spatial distribution. (b) 2PEF, (c) SHG, (d) 3PEF, (e) THG, (f) Five-modal fused ARC image. An enlarged inset highlighting a representative region of interest is provided in Fig. 8(f) to better visualize fine structural and chemical details.

5. Discussion and conclusion

We develop a high-power, tunable dual-wavelength fiber laser source based on SESS technology and demonstrate its application for CARS microscopy. This dual-wavelength source delivers pump pulses continuously tunable from 775 nm to 950 nm. Together with the Stokes pulses fixed at 1.035 μm, this laser source can access a Raman-shift tuning range of 800–3500 cm^{-1} and hence allows access to characteristic vibrational lines of key biomolecules, ranging from DNA and proteins to lipids. We further combine the dual-wavelength CARS source with our previously developed pre-chirp and gain-managed Yb-fiber laser, and employ this combined source to drive MPM imaging with five modalities (*i.e.*, CARS, 2PEF, 3PEF, SHG, and THG). To show the MPM capability, we carry out multimodal imaging of mouse brain slices (D3 V and ARC regions) aiming to highlight the system's chemical selectivity at 2840 cm^{-1} (lipid –C–H stretching) and 3015 cm^{-1} (unsaturated fatty acid = C–H stretching). The CARS image provides clear, specific contrast that complements structural information from SHG, THG, 2PEF, and

Biomedical Optics EXPRESS

3PEF. We further extend the tuning range to the fingerprint region, successfully generating a pump pulse corresponding to ~1700cm^{-1} (amide I band of proteins). However, due to the limited spectral response of the GaAsP PMT detector (cut-off at ~720 nm), the CARS signal at ~765 nm cannot be captured. This technical limitation can be overcome by replacing the detector with a multi-alkali PMT.

In the present implementation of multimodal MPM, the five imaging modalities are realized using two ultrafast laser sources: a pre-chirp and gain-managed Yb-fiber laser source (for exciting SHG, THG, 2PEF, and 3PEF) and a dual-wavelength Er/Yb fiber laser source (for CARS imaging). Although this configuration enables flexible modality switching, broad tunability, high chemical selectivity, and high imaging performance, it inevitably increases system complexity and footprint. Ongoing work is to develop a unified single-source architecture that consolidates all five nonlinear imaging modalities into one coherent laser platform. In this design, a gain-managed Yb-fiber amplifier is used to amplify the 1.035-μm seed of the dual-wavelength system, directly generating 30-fs pulses centered around 1110 nm [46]. A fraction of these pulses is spectrally filtered and temporally stretched to serve as the narrowband Stokes beam and to provide the driving pulses for spectral broadening and filtering required by CARS excitation. Meanwhile, the remaining portion of the same 30-fs pulse train is directly delivered to excite SHG, THG, 2PEF, and 3PEF. By enabling both the coherent Raman and multiphoton excitation channels to originate from a single ultrafast source, this architecture allows all five imaging modalities to be driven by one laser system with inherent spatiotemporal synchronization. Such a scheme significantly simplifies the optical layout, reduces system cost and alignment complexity, and represents an important step toward compact, robust, and clinically deployable multimodal MPM imaging. In addition, while grating-based dispersion compensation is employed in the current laboratory implementation, future engineering-oriented designs may adopt bulk-glass dispersion elements or other alignment-free dispersion management approaches where applicable. Such modifications would further reduce alignment sensitivity and improve environmental ruggedness in field/clinical environments. Looking ahead, the demonstrated fiber-based multimodal platform provides a technical foundation for future imaging of human tissue specimens, particularly in ex vivo label-free histopathology. The broad Raman coverage and multimodal contrast could enable complementary chemical and structural assessment of biopsy samples. Further engineering optimization and validation on clinically relevant specimens will be pursued in future work.

Funding. National Natural Science Foundation of China (92250307, 82573956, 62227822, 62175255); Chinese Academy of Sciences (YJKYYQ20190034).

Disclosures. The authors declare no conflicts of interest.

Data Availability. The data that support the findings of this study are available from the corresponding author upon reasonable request.

References

1. K. M. Hanson and C. J. Bardeen, "Application of nonlinear optical microscopy for imaging skin," Photochem. Photobiol. **85**(1), 33–44 (2009).
2. B. R. Masters, P. T. So, and E. Gratton, "Multiphoton excitation fluorescence microscopy and spectroscopy of in vivo human skin," Biophys. J. **72**(6), 2405–2412 (1997).
3. K. Koenig and I. Riemann, "High-resolution multiphoton tomography of human skin with subcellular spatial resolution and picosecond time resolution," J. Biomed. Opt. **8**(3), 432–439 (2003).
4. S. You, H. Tu, E. J. Chaney, *et al.*, "Intravital imaging by simultaneous label-free autofluorescence-multiharmonic microscopy," Nat. Commun. **9**(1), 2125 (2018).
5. C.-K. Sun, C.-C. Chen, S.-W. Chu, *et al.*, "Multiharmonic-generation biopsy of skin," Opt. Lett. **28**(24), 2488–2490 (2003).
6. Z. Zhang, J. C. de Munck, N. Verburg, *et al.*, "Quantitative third harmonic generation microscopy for assessment of glioma in human brain tissue," Adv. Sci. **6**(11), 1900163 (2019).
7. Y. Farah, G. Murray, J. Field, *et al.*, "Synthetic spatial aperture holographic third harmonic generation microscopy," Optica **11**(5), 693–705 (2024).
8. P. J. Wu, H. C. Tseng, C. C. Chao, *et al.*, "Discontinuity third harmonic generation microscopy for label-free imaging and quantification of intraepidermal nerve fibers," Cells Rep. Methods **4**(3), 100735 (2024).

Biomedical Optics EXPRESS

9. Y. Wu, S. Qiu, M. L. Groot, *et al.*, "Self-Supervised Image Denoising of Third Harmonic Generation Microscopic Images of Human Glioma Tissue by Transformer-Based Blind Spot (TBS) Network," IEEE J. Biomed. Health Inform. **28**(8), 4688–4700 (2024).
10. P. D. Maker and R. W. Terhune, "Study of optical effects due to an induced polarization third order in the electric field strength," Phys. Rev. **137**(3A), A801–A818 (1965).
11. R. F. Begley, A. B. Harvey, and R. L. Byer, "Coherent anti-stokes Raman spectroscopy," Appl. Phys. Lett. **25**(7), 387–390 (1974).
12. X. Nan, A. M. Tonary, A. Stolow, *et al.*, "Intracellular imaging of HCV RNA and cellular lipids by using simultaneous two-photon fluorescence and coherent anti-Stokes Raman scattering microscopies," ChemBioChem **7**(12), 1895–1897 (2006).
13. C. L. Evans, E. O. Potma, M. Puoris'haag, *et al.*, "Chemical imaging of tissue in vivo with video-rate coherent anti-Stokes Raman scattering microscopy," Proc. Natl. Acad. Sci. **102**(46), 16807–16812 (2005).
14. C. L. Evans, X. Xu, S. Kesari, *et al.*, "Chemically-selective imaging of brain structures with CARS microscopy," Opt. Express **15**(19), 12076–12087 (2007).
15. H. Tu and S. A. Boppart, "Coherent anti-Stokes Raman scattering microscopy: overcoming technical barriers for clinical translation," J. Biophotonics **7**(1-2), 9–22 (2014).
16. K. P. Herdzik, K. N. Bourdakos, P. B. Johnson, *et al.*, "Multimodal spectral focusing CARS and SFG microscopy with a tailored coherent continuum from a microstructured fiber," Appl. Phys. B **126**(5), 84 (2020).
17. C. L. Evans and X. Sunney Xie, "Coherent anti-Stokes Raman scattering microscopy: chemical imaging for biology and medicine," Annual Rev. Anal. Chem. **1**(1), 883–909 (2008).
18. K. Inoue and M. Okuno, "Coherent Anti-Stokes Hyper-Raman Spectroscopy," Nat. Commun. **16**(1), 306 (2025).
19. R. Rosser, V. Blanchard, G. Urdaneta Rincon, *et al.*, "Non-equilibrium temperature dynamics in a femtosecond filament using hybrid coherent anti-Stokes Raman scattering," Opt. Lett. **50**(21), 6638–6641 (2025).
20. C. Liu, C. Xiu, Y. Zou, *et al.*, "Cervical cancer diagnosis model using spontaneous Raman and Coherent anti-Stokes Raman spectroscopy with artificial intelligence," Spectrochim. Acta, Part A **327**, 125353 (2025).
21. K. Wang, J. T. Florence, X. Hua, *et al.*, "Coherent Vibrational Anti-Stokes Raman Spectroscopy Assisted by Pulse Shaping," Molecules **30**(10), 2243 (2025).
22. H. Ge, K. Song, M. Xia, *et al.* "Chirped-Probe-Pulse Femtosecond Coherent Anti-Stokes Raman Scattering Thermometry Mapping in Turbulent Flames," J. Raman Spectrosc. (2025).
23. D. Senarathna, H. Achintha Singhapura Singhapurage, and F. Ganikhanov, "Two-wavelength Optical Parametric Oscillator for Time Resolved Coherent Anti-Stokes Raman Spectroscopy," Novel Optical Materials and Applications. Optica Publishing Group 2025.
24. A. Zhitnitsky, E. Benjamin, O. Bitton, *et al.*, "Super-resolved coherent anti-Stokes Raman scattering microscopy by coherent image scanning," Nat. Commun. **15**(1), 10073 (2024).
25. Y. Murakami, N. Sagami, M. Masaki, *et al.*, "Broadband electronic resonance coherent anti-Stokes/Stokes Raman scattering microscopy," bioRxiv (2025).
26. H. Kano and H.-O. Hamaguchi, "Femtosecond coherent anti-Stokes Raman scattering spectroscopy using supercontinuum generated from a photonic crystal fiber," Appl. Phys. Lett. **85**(19), 4298–4300 (2004).
27. H. Song, X. Li, T. Yang, *et al.*, "Exploratory multimodal nonlinear microscopy: Coherent anti-stokes Raman scattering, second harmonic generation, and differential interference contrast for oral squamous cell carcinoma diagnosis," Photodiagn. Photodyn. Ther. **53**, 104577 (2025).
28. J. G. Porquez, R. A. Cole, J. T. Tabarangao, *et al.*, "Spectrally-broad coherent anti-Stokes Raman scattering hyper-microscopy utilizing a Stokes supercontinuum pumped at 800 nm," Biomed. Opt. Express **7**(10), 4335–4345 (2016).
29. M. Brinkmann, A. Fast, T. Hellwig, *et al.*, "Portable all-fiber dual-output widely tunable light source for coherent Raman imaging," Biomed. Opt. Express **10**(9), 4437–4449 (2019).
30. H. Ni, P. Lin, Y. Zhu, *et al.*, "Multiwindow SRS imaging using a rapid widely tunable fiber laser," Anal. Chem. **93**(47), 15703–15711 (2021).
31. Y. Shen, A. A. Voronin, A. M. Zheltikov, *et al.*, "Picosecond supercontinuum generation in large mode area photonic crystal fibers for coherent anti-Stokes Raman scattering microspectroscopy," Sci. Rep. **8**(1), 9526 (2018).
32. C. W. Freudiger, W. Yang, G. R. Holtom, *et al.*, "Stimulated Raman scattering microscopy with a robust fibre laser source," Nat. Photonics **8**(2), 153–159 (2014).
33. C. Kong, C. Pilger, H. Hachmeister, *et al.*, "High-contrast, fast chemical imaging by coherent Raman scattering using a self-synchronized two-colour fibre laser," Light: Sci. Appl. **9**(1), 25 (2020).
34. A. Zach, M. Mohseni, C. Polzer, *et al.*, "All-fiber widely tunable ultrafast laser source for multimodal imaging in nonlinear microscopy," Opt. Lett. **44**(21), 5218–5221 (2019).
35. T. Cao, J. Yan, Y. Chen, *et al.*, "Hybrid CARS spectroscopy based on a high-repetition-rate all-PM-fiber laser source," Appl. Phys. Lett. **117**(8), 081103 (2020).
36. W. Liu, C. Li, Z. Zhang, *et al.*, "Self-phase modulation enabled, wavelength-tunable ultrafast fiber laser sources: an energy scalable approach," Opt. Express **24**(14), 15328 (2016).
37. H. Y. Chung, W. Liu, Q. Cao, *et al.*, "Megawatt peak power tunable femtosecond source based on self-phase modulation enabled spectral selection," Opt. Express **26**(3), 3684 (2018).

Biomedical Optics EXPRESS

38. Y. Hua, G. J. Zhou, W. Liu, *et al.*, "Femtosecond two-color source synchronized at 100-as-precision based on SPM-enabled spectral selection," Opt. Lett. **45**(13), 3410 (2020).
39. Y. Liu, H. Tu, S. You, *et al.*, "Label-free molecular profiling for identification of biomarkers in carcinogenesis using multimodal multiphoton imaging," Quant. Imaging Med. Surg **9**(5), 742 (2019).
40. Y. Liu, J. Zhao, Z. Wei, *et al.*, "High-power, high-repetition-rate tunable longwave mid-IR sources based on DFG in the OPA regime," Opt. Lett. **48**(4), 1052–1055 (2023).
41. T. Hellerer, A. M. Enejder, and A. Zumbusch, "Spectral focusing: High spectral resolution spectroscopy with broad-bandwidth laser pulses," Appl. Phys. Lett. **85**(1), 25–27 (2004).
42. M. Mohseni, C. Polzer, and T. Hellerer, "Resolution of spectral focusing in coherent Raman imaging," Opt. Express **26**(8), 10230–10241 (2018).
43. J.-X. Cheng, Y. Kevin Jia, G. Zheng, *et al.*, "Laser-scanning coherent anti-Stokes Raman scattering microscopy and applications to cell biology," Biophys. J. **83**(1), 502–509 (2002).
44. Y. Xing, R. Chen, L. Zhang, *et al.*, "SLAM medical imaging enabled by a pre-chirp and gain jointly managed Yb-fiber laser," Biomed. Opt. Express **15**(2), 911–923 (2024).
45. C. Heinrich, A. Hofer, A. Ritsch, *et al.*, "Selective imaging of saturated and unsaturated lipids by wide-field CARS-microscopy," Opt. Express **16**(4), 2699–2708 (2008).
46. P. Sidorenko, W. Fu, and F. Wise, "Nonlinear ultrafast fiber amplifiers beyond the gain-narrowing limit," Optica **6**(10), 1328–1333 (2019).